

A global stability approach to wake and path instabilities of nearly oblate spheroidal rising bubbles

José Carlos Cano-Lozano, Joël Tchoufag, Jacques Magnaudet, Carlo Martínez-Bazán

► To cite this version:

José Carlos Cano-Lozano, Joël Tchoufag, Jacques Magnaudet, Carlo Martínez-Bazán. A global stability approach to wake and path instabilities of nearly oblate spheroidal rising bubbles. *Physics of Fluids*, American Institute of Physics, 2016, vol. 28 (n° 1), pp. 014102. <10.1063/1.4939703>. <hal-01330745>

HAL Id: hal-01330745

<https://hal.archives-ouvertes.fr/hal-01330745>

Submitted on 13 Jun 2016

HAL is a multi-disciplinary open access archive for the deposit and dissemination of scientific research documents, whether they are published or not. The documents may come from teaching and research institutions in France or abroad, or from public or private research centers.

L'archive ouverte pluridisciplinaire **HAL**, est destinée au dépôt et à la diffusion de documents scientifiques de niveau recherche, publiés ou non, émanant des établissements d'enseignement et de recherche français ou étrangers, des laboratoires publics ou privés.



Open Archive TOULOUSE Archive Ouverte (OATAO)

OATAO is an open access repository that collects the work of Toulouse researchers and makes it freely available over the web where possible.

This is an author-deposited version published in: <http://oatao.univ-toulouse.fr/>
Eprints ID : 15911

To link to this article : DOI:10.1063/1.4939703

URL : <http://dx.doi.org/10.1063/1.4939703>

To cite this version :

Cano-Lozano, José Carlos and Tchoufag, Joël and Magnaudet, Jacques and Martínez-Bazán, Carlo *A global stability approach to wake and path instabilities of nearly oblate spheroidal rising bubbles*. (2016) Physics of Fluids, vol. 28 (n° 1). pp. 014102. ISSN 1070-6631

Any correspondence concerning this service should be sent to the repository administrator: staff-oatao@listes-diff.inp-toulouse.fr

A global stability approach to wake and path instabilities of nearly oblate spheroidal rising bubbles

José Carlos Cano-Lozano,¹ Joël Tchoufag,² Jacques Magnaudet,^{2,3}
and Carlos Martínez-Bazán¹

¹*Área de Mecánica de Fluidos, Departamento de Ingeniería Mecánica y Minera, Universidad de Jaén, Campus de las Lagunillas, 23071 Jaén, Spain*

²*Université de Toulouse, INPT, UPS, IMFT (Institut de Mécanique des Fluides de Toulouse), Allée Camille Soula, F-31400 Toulouse, France*

³*CNRS; IMFT, F-31400 Toulouse, France*

(Received 25 September 2015; accepted 27 December 2015; published online 12 January 2016)

A global Linear Stability Analysis (LSA) of the three-dimensional flow past a nearly oblate spheroidal gas bubble rising in still liquid is carried out, considering the actual bubble shape and terminal velocity obtained for various sets of Galilei (Ga) and Bond (Bo) numbers in axisymmetric numerical simulations. Hence, this study extends the stability analysis approach of Tchoufag *et al.* [“Linear stability and sensitivity of the flow past a fixed oblate spheroidal bubble,” *Phys. Fluids* **25**, 054108 (2013) and “Linear instability of the path of a freely rising spheroidal bubble,” *J. Fluid Mech.* **751**, R4 (2014)] (which considered perfectly spheroidal bubbles with an arbitrary aspect ratio) to the case of bubbles with a realistic fore-aft asymmetric shape (i.e., a flatter front and a more rounded rear). The critical curve separating stable and unstable regimes for the straight vertical path is obtained both in the (Ga, Bo) and the (Re, χ) planes, where Re is the bubble Reynolds number and χ its aspect ratio (i.e., the major-to-minor axes length ratio). This provides new insight into the effect of the shape asymmetry on the wake instability of bubbles held fixed in a uniform stream and on the path instability of freely rising bubbles, respectively. For the range of Ga and Bo explored here, we find that the flow past a bubble with a realistic shape is generally more stable than that past a perfectly spheroidal bubble with the same aspect ratio. This study also provides the first critical curve for the onset of path instability that can be compared with experimental observations. The tendencies revealed by this critical curve agree well with those displayed by available data. The quantitative agreement is excellent for $O(1)$ Bond numbers. However, owing to two simplifying assumptions used in the LSA scheme, namely, the steadiness of the base state and the uncoupling between the bubble shape and the flow disturbances, quantitative discrepancies (up to 20%–30%) with experimental threshold values of the Galilei number remain for both small and large Bond numbers. © 2016 AIP Publishing LLC. [<http://dx.doi.org/10.1063/1.4939703>]

I. INTRODUCTION

Bubble rising in a quiescent liquid is a phenomenon of key interest in multiple environmental, geophysical, and industrial contexts. The corresponding dynamics, i.e., the evolution of the bubble shape, the path that the bubble describes as it rises in a still liquid, and the topology of its wake have been widely studied experimentally and numerically.^{3–6} However, from the experimental point of view, it remains a challenge to obtain quantitative data using ultrapure water.^{7,8} The addition of surfactants affects the dynamics of the gas-liquid interface, changing the shear-free condition into a no-slip one and altering, as a result, the path and wake of the bubble.^{9,10} Moreover, the presence of surfactants is known to increase the drag and hence decrease the critical Reynolds number (based on the equivalent diameter and terminal rise velocity of the bubble) and the critical aspect ratio beyond which the bubble path becomes unstable and departs from a vertical straight line. This is because more vorticity is produced at the interface for a given rise velocity, i.e., a given Reynolds

number, when the shear-free condition is changed into a no-slip one. It is now well established (see Ref. 11) that, for both solid bodies and bubbles, wake instability occurs when the amount of vorticity produced at the surface exceeds some critical value. Hence, the vorticity threshold is reached with a lower Reynolds number when the bubble surface is contaminated. Surfactant effects may be eliminated by using nonpolar liquids, especially silicon oils.^{12,13} However, silicon oils have low surface tensions (typically four times lower than water), resulting in significant bubble deformations even for bubbles of small size. This limits somewhat the possibility to use them to explore in detail the stability of the flow past moderately deformed bubbles, since the reduced size of the latter (compared to similar bubbles in water) increases the difficulty to obtain accurate measurements in the wake (e.g., through particle image velocimetry). Whatever the selected carrying liquid, determining accurately the above critical parameters from experiments is not a trivial task: it requires sophisticated optical devices in at least two orthogonal planes, and a long tank because in certain regimes the bubble may travel a long distance before its path displays an instability. This is why experimental results may contain non-negligible errors if the tank used is not sufficiently long.¹⁴

In order to avoid the inconveniences or go beyond the limitations mentioned above, Direct Numerical Simulation (DNS) has been increasingly used in the recent years to analyze the structure and stability of the flow induced by the bubble motion.^{11,15,16} These studies succeeded in determining the thresholds for the transition from straight to zig-zag bubble path though, in most cases, the bubble shape was considered fixed during its motion. Recently, Linear Stability Analysis (LSA) has also been proposed as a powerful tool to determine the neutral curves for wake^{1,17} and path² instabilities.

In the present study, we use LSA to determine the transition to instability of the flow past a rising bubble using a realistic bubble shape, thus going a step further than the previous aforementioned works where a spheroidal shape was prescribed. We consider two different configurations, namely, the case of bubbles held fixed in a uniform stream on the one hand and that of freely rising bubbles on the other hand. Through this, we are able to analyze the influence of the fore-aft asymmetry of the bubble shape on the stability properties of the surrounding flow and of the bubble path. The present paper is organized as follows. Section II describes the LSA procedure and the results obtained through it with a fixed bubble exhibiting fore-aft asymmetry. Then, Section III deals with freely moving bubbles with such an asymmetry and compares the corresponding LSA results with those obtained in Ref. 2 assuming perfectly spheroidal bubbles. Section IV summarizes the main results and remaining issues, opening the door to questions to be addressed in a future work.

II. LSA OF THE FLOW PAST FIXED FORE-AFT ASYMMETRIC BUBBLES

We focus here on the wake instability of bubbles whose shape, velocity, and orientation are kept fixed once an equilibrium shape and a terminal velocity have been reached in an axisymmetric computation. We assess wake instability by means of the LSA approach. Two different codes are used in a complementary manner to carry out the study: the Gerris Flow Solver^{18,19} provides the final shape and rise velocity, while FreeFem++²⁰ is employed to achieve the LSA. The former is a finite volume multiphase solver in which interfaces are tracked using a Volume of Fluid (VOF) technique combined with a quad/octrees discretization, while the latter is based on the finite element method.

A. Problem configuration and methodology

The selected control parameters are the Galilei number, $Ga = \rho D \sqrt{gD} / \mu$ (also frequently referred to as the Archimedes number), and the Bond number, $Bo = \rho g D^2 / \sigma$, where ρ is the liquid density, D the equivalent bubble diameter such that the bubble volume equals $\pi D^3 / 6$, g is the gravitational acceleration, μ the liquid viscosity, and σ the surface tension. These two dimensionless parameters are related to the Morton number, $Mo = g \mu^4 / \rho \sigma^3$, which only depends on the fluid properties through $Mo = Bo^3 / Ga^4$, so that they are indeed sufficient to characterize entirely the bubble shape and velocity.¹⁶ Note that, similar to the Reynolds number $Re = \rho U_T D / \mu$, the aspect

ratio χ is not, strictly speaking, a control parameter but an outcome of the simulation for a given set (Ga, Bo) . Therefore, a given value of χ may correspond to bubbles with different shapes.¹⁶

It must be realized that, for the time being, no DNS code is capable of performing a LSA of the flow past a freely evolving fluid-fluid interface. There is now a good number of incompressible DNS codes providing accurate predictions of the flow and interface shape in various two-phase configurations but, to the best of our knowledge, none of them comprise a linearized version with the dedicated routines and algorithms required to achieve LSA. Conversely, none of the available LSA codes offer the possibility to compute the base flow around an interface whose shape is determined by the flow itself. Therefore, in such situations, LSA codes must be “fed” with an initial solution provided by a separate multiphase DNS code. This state of affairs led us to use two separate codes.

We first employ the Gerris Flow Solver to compute the bubble shape and terminal velocity, U_T , corresponding to the base state by means of axisymmetric direct numerical simulations of the full Navier-Stokes equations. For this purpose, we use the configuration already validated in previous works,^{16,21} starting the simulations with a spherical bubble in a fluid at rest and considering gas-to-liquid density and viscosity ratios of 10^{-3} and 10^{-2} , respectively. Then, the bubble acquires its actual shape as it rises under buoyancy, until it eventually reaches a terminal velocity. The simulations are stopped when the terminal velocity and the shape are steady, i.e., remain unchanged over time (up to a certain precision lower than 1% for both U_T and χ).²¹ The accuracy of the corresponding predictions, namely, U_T and the bubble shape, was discussed in detail in Ref. 16. Table 4 of that reference indicates for instance that in the case of a bubble with $Ga = 239, Bo = 0.44$ rising in pure water (a situation which was considered experimentally in Ref. 8 and was found to correspond to a marginally stable bubble), the computational predictions differ from the experimental observations by 0.17% for the terminal velocity and 3.5% for the aspect ratio. Comparisons with experiments performed in different silicon oils revealed a similar agreement. This good agreement with experimental data corresponding to contrasting conditions validates the first step of the present approach.

In a second step, we use FreeFem++ to perform the LSA of the flow about the bubble whose shape and terminal velocity have been previously obtained. In FreeFem++, the flow is governed by the incompressible Navier-Stokes equations which, using D and U_T as characteristic length and velocity scales, respectively, read in dimensionless form

$$\nabla \cdot \mathbf{U} = 0, \quad (1)$$

$$\partial_t \mathbf{U} + \mathbf{U} \cdot \nabla \mathbf{U} = \nabla \cdot \mathbf{T}, \quad (2)$$

where ∂_t denotes the partial time derivative, $\mathbf{T} = -P\mathbf{I} + Re^{-1}(\nabla \mathbf{U} + \nabla \mathbf{U}^T)$ is the stress tensor, \mathbf{I} the Kronecker tensor, and Re the Reynolds number defined as $Re = \rho D U_T / \mu$ (note that gravity is not involved in (2) since the bubble is held fixed). The flow is forced by imposing a unit velocity through the upper boundary of the domain, ∂_{in} (see Figure 1). In addition, dynamic and kinematic boundary conditions are imposed at the bubble surface, ∂_b . This is achieved by assuming that the bubble does not deform any more after it has reached its terminal velocity (i.e., its shape is not altered by the small-amplitude pressure disturbances considered in the LSA approach) and that the viscosity of the gas that fills it is negligibly small, so that the continuity of shear stresses forces the outer fluid to satisfy a zero-shear condition at the bubble surface. These two conditions simply read

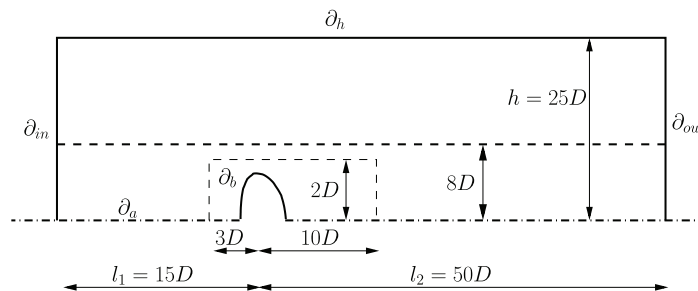


FIG. 1. Sketch of the domain employed in the simulations performed with FreeFem++.

$$\mathbf{n} \times (\mathbf{T} \cdot \mathbf{n}) = 0, \quad (3)$$

$$\mathbf{U} \cdot \mathbf{n} = 0, \quad (4)$$

where \mathbf{n} denotes the outward unit normal at the surface.

The flow is then classically split into the so-called base flow plus infinitely small disturbances (of order ϵ) around it. The bubble shape obtained with Gerris is frozen and the base flow past the bubble held fixed is determined with FreeFem++, using the terminal velocity obtained with Gerris as the speed of the incoming stream. Then, at order ϵ , the linearized perturbation problem resulting from (1)-(4) is solved to evaluate the stability of the previously computed base flow (see the computational domain sketched in Figure 1). The finite element technique, with quadratic (respectively, linear) elements for interpolating the velocity (respectively, pressure) fields, is used to solve the $O(1)$ and $O(\epsilon)$ problems. More details on the weak formulation of the equations are given in Appendix A of Ref. 1.

B. Base flow problem

1. Governing equations

Following the LSA approach of Ref. 1, we look for a strictly steady, axisymmetric base solution of governing system (1)-(4). It can be shown²² that a proper finite element formulation of the Navier-Stokes equations with a slip boundary condition requires the normal stress Σ at the corresponding surface to be added to the usual unknown velocity and pressure fields. Therefore, the governing equations of the base flow (characterized by velocity and pressure fields \mathbf{U}_0 and P_0 , respectively) to be solved in the cylindrical domain displayed in Figure 1 read

$$\nabla \cdot \mathbf{U}_0 = 0, \quad (5)$$

$$\mathbf{U}_0 \cdot \nabla \mathbf{U}_0 = \nabla \cdot \mathbf{T}_0, \quad (6)$$

$$\mathbf{T}_0 \cdot \mathbf{n} = \Sigma_0 \mathbf{n} \quad \text{on} \quad \partial_b, \quad (7)$$

$$\mathbf{U}_0 \cdot \mathbf{n} = 0 \quad \text{on} \quad \partial_b, \quad (8)$$

$$\mathbf{U}_0 = \mathbf{e}_x \quad \text{on} \quad \partial_{in}, \quad (9)$$

$$\mathbf{T}_0 \cdot \mathbf{n} = \mathbf{0} \quad \text{on} \quad \partial_{out}, \quad (10)$$

$$\mathbf{e}_r \cdot \mathbf{U}_0 = (\mathbf{e}_r \cdot \nabla)(\mathbf{U}_0 \cdot \mathbf{e}_x) = 0 \quad \text{on} \quad \partial_a \cup \partial_h, \quad (11)$$

where Σ_0 denotes the base normal stress at the bubble surface, and \mathbf{e}_x and \mathbf{e}_r are the unit vectors in the streamwise and radial directions, respectively. Equation (11) expresses the symmetry condition on the domain axis and the shear-free condition on its lateral boundary. The system being nonlinear, the base flow solution is approached using an iterative Newton method, as described in Ref. 23.

2. Validation of the base flow

The base flow (and the $O(\epsilon)$ problem to be described later) was solved on the computational domain sketched in Figure 1. This domain was discretized into triangular elements via a Delaunay-Voronoi algorithm. The corresponding grid was refined in a region close to the bubble ($3D$ ahead of it and $10D$ behind it) to make sure that the near wake is adequately resolved. The domain size and grid refinement were first validated by comparing results with those of previous studies devoted to spheroidal bubbles.¹ As shown in Table I, predictions for the drag coefficient are in excellent agreement with those of Ref. 1.

Furthermore, the base flow was compared with results provided by Gerris regarding the velocity and pressure fields and the development of a standing eddy at the rear of the bubble. Figure 2 shows that the pressure and velocity fields produced by the two codes are very close, although some tiny differences may be discerned in the near wake. The drag coefficients C_D provided by FreeFem++ were also compared with the quantity $C_{DG} = 4Ga^2/3Re^2$ provided by Gerris: indeed, C_{DG} is the drag coefficient resulting from a balance between buoyancy and viscous forces. This

TABLE I. Drag coefficient C_D corresponding to a steady axisymmetric flow past a spheroidal bubble; C_D is defined as $8F_x/\pi$, where F_x denotes the dimensionless drag force.

χ	1			1.75			2.25		
Re	100	400	1000	166	332	830	100	500	1000
Present study	0.3742	0.1066	0.0446	0.5184	0.2853	0.1217	1.0975	0.3048	0.1582
Tchoufag <i>et al.</i> ¹	0.374	0.107	0.045	0.518	0.285	0.122	1.097	0.305	0.158

comparison revealed a relative error lower than 5%, thus confirming the good agreement between the two codes.

C. Perturbation problem

1. Governing equations

At order ϵ , the governing equations for the disturbances are obtained by linearizing the Navier-Stokes equations and the boundary conditions around the base state. The former read

$$\nabla \cdot \mathbf{u} = 0, \quad (12)$$

$$\partial_t \mathbf{u} + \mathbf{u} \cdot \nabla \mathbf{U}_0 + \mathbf{U}_0 \cdot \nabla \mathbf{u} = \nabla \cdot \mathbf{t}, \quad (13)$$

where $\mathbf{t} = -p\mathbf{I} + Re^{-1}(\nabla \mathbf{u} + \nabla \mathbf{u}^T)$ is the stress tensor disturbance. Equations (12) and (13) must be solved and are subjected to the boundary conditions

$$\mathbf{t} \cdot \mathbf{n} = \sigma_s \mathbf{n} \quad \text{on} \quad \partial_b, \quad (14)$$

$$\mathbf{u} \cdot \mathbf{n} = 0 \quad \text{on} \quad \partial_b, \quad (15)$$

$$\mathbf{u} = \mathbf{0} \quad \text{on} \quad \partial_{in} \cup \partial_h, \quad (16)$$

$$\mathbf{t} \cdot \mathbf{n} = \mathbf{0} \quad \text{on} \quad \partial_{out}, \quad (17)$$

where σ_s is the disturbance of the normal stress at the bubble surface. The boundary condition on the axis ∂_a depends on the symmetry of the mode under consideration. The solution of the linearized problem is sought in the form of normal modes. We take advantage of the axisymmetric geometry of the flow domain to expand this solution in Fourier modes in the azimuthal direction θ . Hence, the state vector $\mathbf{q} = (\mathbf{u}, p, \sigma_s)$ reads in the cylindrical (r, θ, x) coordinate system as

$$\mathbf{q} = \hat{\mathbf{q}}(r, x)e^{\lambda t + im\theta} + c.c., \quad (18)$$

where $c.c.$ denotes the complex conjugate. In this expansion, $\lambda = \lambda_r + i\lambda_i$ is the complex eigenvalue whose real (imaginary) part is the perturbation growth rate (frequency), m being the azimuthal

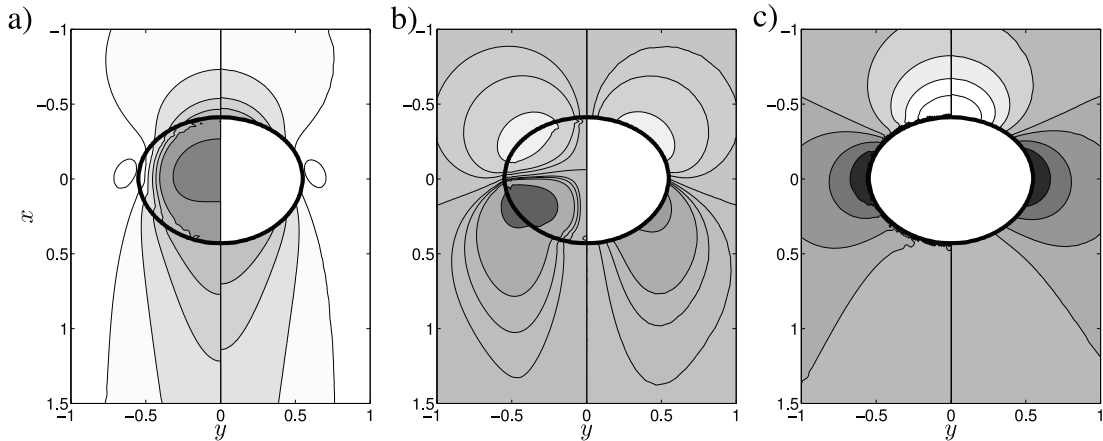


FIG. 2. Comparison of the base flow obtained with Gerris (left) and FreeFem++ (right) for a bubble with $Bo = 1$ and $Ga = 50$. Iso-contours of dimensionless (a) axial velocity $[-1, -0.5, 0.0, 0.2, 0.4, 0.7, 0.9, 1.0, 1.2]$, from dark to light, (b) radial velocity $[-1.0, -0.25, -0.1, -0.07, -0.04, 0.0, 0.08, 0.15, 0.4]$, and (c) pressure $[-0.6, -0.3, -0.15, -0.05, 0.0, 0.1, 0.2, 0.3, 0.4]$.

wavenumber. The stability analysis is restricted to $m = \pm 1$, since it has been established previously that these are the most unstable modes.^{1,11} Therefore, the appropriate boundary conditions on the domain axis ∂_a read

$$\mathbf{e}_x \cdot \hat{\mathbf{u}} = (\mathbf{e}_r \cdot \nabla)(\hat{\mathbf{u}} \cdot \mathbf{e}_r) = \hat{p} = 0. \quad (19)$$

Once the normal modes decomposition has been injected into the linearized equations, systems (12)-(17) and (19) can be recasted in the form of a generalized eigenvalue problem

$$\lambda \mathcal{B} \hat{\mathbf{q}} + \mathcal{A} \hat{\mathbf{q}} = \mathbf{0}, \quad (20)$$

where \mathcal{B} and \mathcal{A} are the mass and stiffness matrices, respectively. In FreeFem++, these matrices are built using the UMFPAK library. The eigenvalue problem (20) is solved using a shift-invert Arnoldi technique implemented in the SLEPc library (<http://www.grycap.upv.es/slepc/>).

2. LSA results: Influence of the bubble shape on wake instability

The LSA results showing the neutral curve obtained in the case of a fixed bubble with fore-aft asymmetry are displayed in the plane of the control parameters in Figure 3. For such a fixed body, the neutral curve separates regions of the parameter space where the axisymmetric wake is linearly stable or unstable. In Figure 3(a), these results are compared with those obtained in Ref. 1 for a perfectly spheroidal bubble. In this case, the relevant control parameters are the bubble aspect ratio, χ , and the Reynolds number, Re , since the shape is prescribed and does not evolve with the Reynolds number. The neutral curve is also shown in Figure 3(b) in the “natural” (Ga, Bo) plane, together with the bubble cross section at three selected locations. For these three bubbles, the fore-aft asymmetry in the order of increasing Bo is 34%, 32%, and 48%, respectively, i.e., it is a non-monotonic function of the Bond number.

It appears that the fore-aft asymmetry has a non-negligible influence on the stability of the wake. More specifically, for a given aspect ratio larger than the critical value $\chi_c \approx 2.215$ corresponding to the “nose” of the neutral curve, it is seen to decrease the range of Re within which the wake is unstable, by moving the upper branch down. For instance, considering a bubble corresponding to point P_u in Figure 3(a), with an aspect ratio $\chi = \chi_u = 2.306$ and a Reynolds number $Re_u = 888.55$, it turns out that the flow past the real bubble is stable, while that past a perfectly spheroidal bubble is neutrally unstable. In contrast, shape asymmetry leaves the lower branch of the neutral curve almost unaffected; we shall discuss the reason for this weak influence later.

In physical terms, the stabilizing effect of the shape asymmetry may be understood by noting that, starting from an oblate spheroidal shape, flattening the front part and rounding the rear part may be obtained by imposing some slow suction on the former and some slow blowing on the latter (designed such that the total flow rate through the bubble surface is zero in order to keep its volume constant). Suction is known to make a boundary layer thinner and stabilize it, and so does

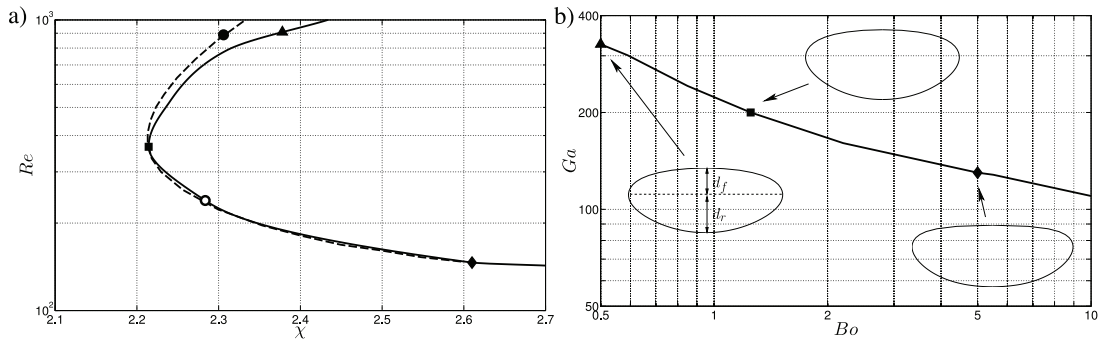


FIG. 3. Neutral curves obtained from the LSA in the case of a fixed bubble: (a) comparison in the (χ, Re) plane between present results corresponding to a real bubble shape (solid line) and results from Ref. 1 for a spheroidal shape (dashed line). (b) Neutral curve in the (Bo, Ga) plane for a real bubble shape. In (a), the triangle, square and lozenge symbols identify the (χ, Re) coordinates of the three bubbles whose shape is displayed in (b); for these three bubbles, the ratio d_f/d_r defined in the figure, which is a measure of the fore-aft asymmetry, is 0.66, 0.68, and 0.52, respectively. The bullet (\bullet) and the circle (\circ) in (a) identify the points P_u and P_l discussed in the text, respectively.

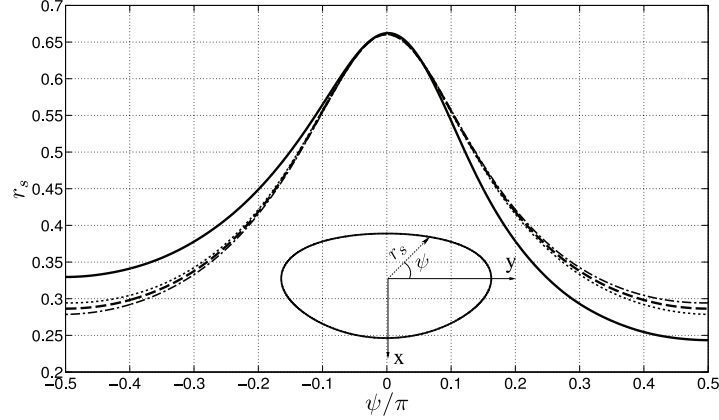


FIG. 4. Different bubble shapes, all corresponding to $\chi = \chi_u$, in polar coordinates. The solid line shows the real bubble shape, while the dashed line shows the perfectly spheroidal bubble. The dotted and dashed-dotted lines represent bubbles whose shape is close to a spheroid but with a slightly flatter front and more rounded rear and a more rounded front and slightly flatter rear, respectively.

the flattening of the front part on the boundary layer that develops from the front stagnation point of the bubble toward its equatorial plane. Blowing is also known to stabilize the near wake of bluff bodies by reducing or even suppressing the standing eddy that takes place there, thus weakening the source of wake instability.^{24,25} Oblate bubbles are basically bluff bodies on which most of the vorticity is produced in the vicinity of the equatorial plane ($\psi = 0$ in Figure 4) which is the part of the surface where the curvature reaches its maximum.¹¹ On these grounds one can expect that, for a given curvature of the surface in the equatorial plane, making the rear part of the bubble more rounded stabilizes its wake. Hence, both mechanisms cooperate to make the flow past the bubble more stable.

In order to better understand the influence of the bubble shape, we select conditions corresponding to point P_u in Figure 3(a), to carry out the LSA of the flow past several bubbles with slightly different shapes. The various bubble shapes we considered are displayed in Figure 4 in polar coordinates. Four different shapes are investigated, including the “real” shape computed from Gerris and the spheroidal one. The other shapes were obtained by slightly deforming either the front or the rear of the spheroidal bubble, thus inducing a controlled fore-aft asymmetry. These shape alterations, resulting in a flatter front and a more rounded rear (or vice versa), were kept small in order to maintain the bubble volume constant. By this means, the equivalent diameter (and thus all dimensionless parameters) remains unchanged, allowing us to isolate the particular influence of the bubble shape. Figure 5 shows the eigenvalue spectra obtained with the four different shapes. It appears that, for the same value of the aspect ratio, the flow past the real-shape bubble

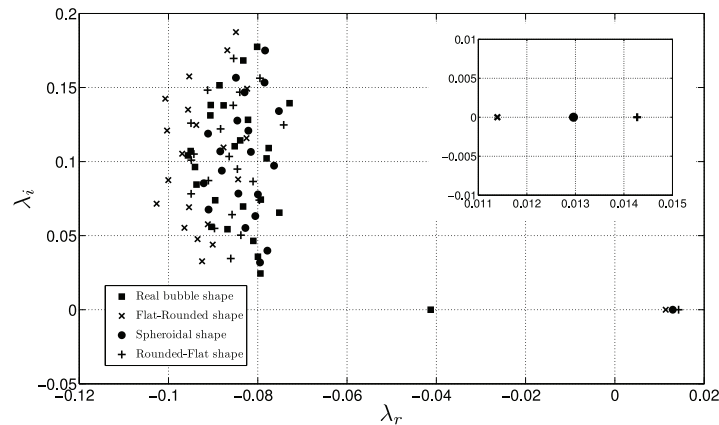


FIG. 5. Eigenvalue spectrum for different bubble shapes, all corresponding to point P_u in Figure 3(a). The inset shows the growth rates (λ_r) of the three unstable modes, respectively, obtained with the spheroidal, rounded-flat, and flat-rounded bubbles.

is more stable than any of the other three. Moreover, we observe that the flow past a bubble with a slightly flatter front and a slightly more rounded rear, referred to as “*flat-rounded*” in the caption of Figure 5, is somewhat more stable than that past the spheroidal bubble. Not unlikely, the opposite is observed in the case of a bubble with a slightly more rounded front and a slightly flatter rear (referred to as “*rounded-flat*”). These conclusions are in line with those of the sensitivity analysis carried out in Ref. 1 for perfectly spheroidal bubbles. There it was shown that a positive normal velocity disturbance applied to the bubble surface (hence leading to a local increase of the bubble radius) is destabilizing (stabilizing) when applied on the front (rear) part of the surface. Of course Figure 5 also agrees with the latter work in that it confirms that for both spheroidal and fore-aft asymmetric bubbles, the primary wake instability occurs through a stationary bifurcation (i.e., with $\lambda_i = 0$). In Ref. 1, the full LSA diagram in the (χ, Re) plane also contains a branch defining a region where the axisymmetric wake becomes unstable through an unsteady (Hopf) bifurcation. We did not plot this branch here, although it also exists with real-shape bubbles, for two main reasons. First of all, only the first bifurcation can allow a direct comparison with experiments, except when the stationary and Hopf bifurcations occur within a small Re interval, a situation which may result in nonlinear modes interaction and resonance. Second, in the region $\chi \geq 2.41$ where the flow is unstable to unsteady modes in the case of a spheroidal bubble, the Weber number $We = Bo(Re/Ga)^2$ comparing the inertia and surface tension effects is typically large enough to induce some wobbling of the bubble. Therefore, as we assume that the bubble shape remains unaffected by the disturbance, conclusions drawn in that regime would be somewhat questionable.

To finish with the fixed-bubble case, it is of interest to understand why the influence of the fore-aft shape asymmetry on the flow stability is much stronger along the upper branch of the neutral curve than along the lower one. To elucidate this point, one has to look at the vorticity distribution and streamline pattern around the corresponding bubbles. These quantities are displayed in Figure 6 for two sets of bubbles with almost identical aspect ratios. One corresponds to the point P_u examined above, the other to the point P_l in Figure 3(a), i.e., $\chi_l = 2.28, Re_l = 239$. Hence, the two sets have almost identical aspect ratios, with the former (latter) standing on the upper (lower) branch of the neutral curve determined for spheroidal bubbles. In each set, examination of the surface vorticity distribution (not shown) indicates that the maximum vorticity is essentially the same on the fore-aft asymmetric bubble and on the perfectly spheroidal one. Hence, as could be

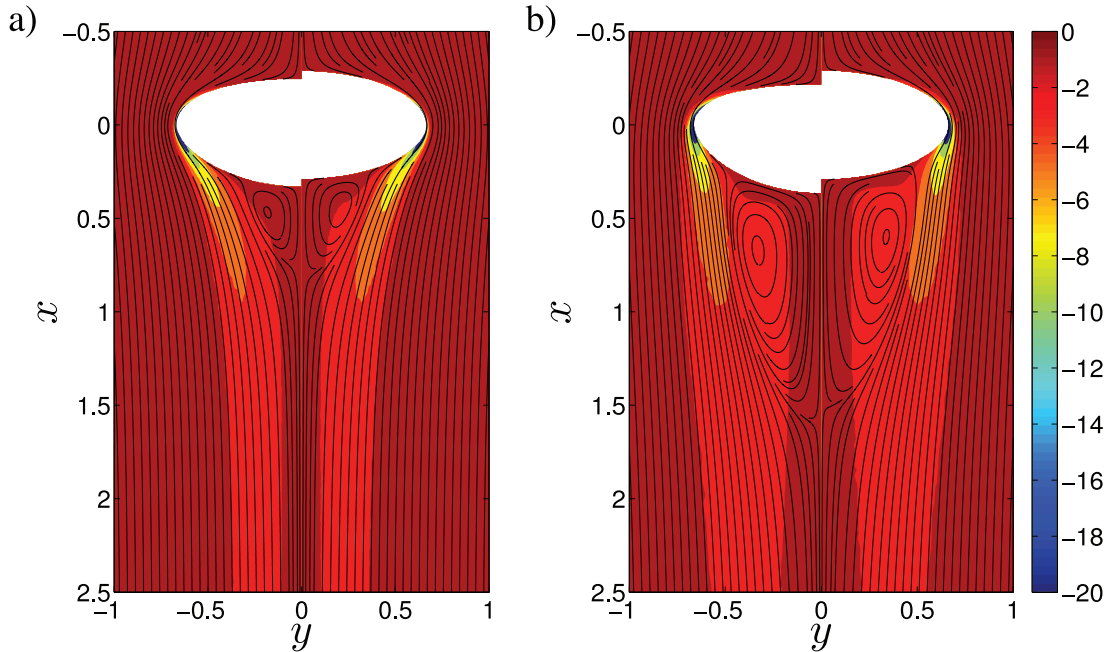


FIG. 6. Azimuthal vorticity distribution (color scale) and streamline pattern past a spheroidal bubble (right half) and a fore-aft asymmetric bubble with the same aspect ratio (left half); the equatorial plane of the two bubbles stands on the same line ($x = 0$), unlike the front and rear stagnation points. (a) Point P_u on the upper branch; (b) point P_l on the lower branch.

anticipated, surface vorticity appears to be almost insensitive to the precise shape of the front and rear parts, provided the curvature is unchanged near the equatorial plane. Once generated at the bubble surface, vorticity diffuses throughout the boundary layer and is advected downstream. This is where the precise structure of the streamline pattern comes into play. Indeed, as the Reynolds number increases, advection becomes more and more dominant compared to viscous diffusion, and the precise shape of the streamlines influences the amount of vorticity that is brought to a specific location in the near wake. Consider the downstream part of streamlines that pass close to the bubble surface in the equatorial plane. A bubble with a rounded rear being somewhat more elongated than a spheroidal one in the direction of the main stream, the corresponding streamlines are slightly less inclined towards the symmetry axis. Hence, somewhat less vorticity is released near the rear stagnation point, unless viscous diffusion is able to compensate for this shape effect. With this scenario in mind, for a given (χ, Re) set and a large enough Re , one expects the standing eddy to be somewhat smaller and less intense in the case of a fore-aft asymmetric bubble. As the source of the (absolute) wake instability stands in this eddy,¹ it can be guessed that the fore-aft asymmetry tends to make the flow more stable. This is exactly what is observed at P_u . Indeed, Figure 6(a) reveals a significant reduction of the size of the standing eddy in the case of an asymmetric shape. In contrast, this size is virtually unaffected by the asymmetry at P_l , although this asymmetry is actually larger than at P_u (compare the shapes at points A and C in Figure 9(b)). This is because vorticity can still reach the rear stagnation point region thanks to viscous diffusion, the Reynolds number at P_l being nearly four times smaller than at P_u . Hence, it turns out that the stabilizing effect of the shape asymmetry is barely felt on the lower branch of the neutral curve, being neutralized by viscous diffusion.

III. LSA OF THE FLOW PAST FREELY RISING BUBBLES WITH FORE-AFT ASYMMETRY

We now turn to the configuration where the bubble is no longer fixed but instead is free to rise under buoyancy. As in the previous configuration, we consider bubbles whose shapes are obtained with Gerris for a given set of Ga and Bo , and then use FreeFem++ to analyze the stability of their initially vertical trajectory. This vertical rise is investigated following a recent approach^{2,26} which is able to predict the stability fate of axisymmetric bodies by carrying out the LSA of the fully coupled fluid+body system.

A. Problem formulation

Following the aforementioned studies, we introduce a system of axes (x, y, z) translating and rotating with the bubble, x being aligned with its minor axis. We express the fluid problem using a cylindrical coordinate system (r, θ, x) related to the Cartesian coordinates (x, y, z) through $y = r \cos \theta$, $z = r \sin \theta$. The set of equations governing the moving bubble in a fluid otherwise at rest is made of the Navier-Stokes equations for the fluid and the Newton equations expressing momentum and moment of momentum conservation for the bubble. In the latter two, we assume that the gas that fills the bubble has a negligibly small density, so that we neglect the bubble mass and moment of inertia. Written in an absolute reference frame and projected onto the (x, y, z) axes, the corresponding system of governing equations reads

$$\nabla \cdot \mathbf{U} = 0, \quad (21)$$

$$\partial_t \mathbf{U} + (\mathbf{U} - \mathbf{W}) \cdot \nabla \mathbf{U} + \boldsymbol{\Omega} \times \mathbf{U} = \nabla \cdot \mathbf{T}, \quad (22)$$

$$\int_s \mathbf{T} \cdot \mathbf{n} dS = \frac{\pi}{6} \mathbf{g}, \quad (23)$$

$$\int_s \mathbf{r} \times (\mathbf{T} \cdot \mathbf{n}) dS = \mathbf{0}, \quad (24)$$

$$\frac{d\boldsymbol{\Xi}}{dt} = \boldsymbol{\Omega}, \quad (25)$$

where $\mathbf{W} = \mathbf{V} + \boldsymbol{\Omega} \times \mathbf{r}$ is the local entrainment velocity, \mathbf{V} and $\boldsymbol{\Omega}$ being the translational and rotational bubble velocities, respectively, and \mathbf{r} the local position vector measured from the geometrical

centre of the bubble. Equation (25) relates at any time the rotation rate $\mathbf{\Omega}$ to the bubble orientation vector $\mathbf{\Xi}$ whose components are the roll/pitch/yaw angles with respect to a system of axes with a fixed orientation (x_0, y_0, z_0) (see Refs. 2 and 26 for more details). Equations (21)-(25) have been made dimensionless using $(gD)^{1/2}$ as characteristic velocity (instead of U_T in Section II). Consequently, the dimensionless stress tensor is now $\mathbf{T} = -P\mathbf{I} + Ga^{-1}(\nabla\mathbf{U} + \nabla\mathbf{U}^T)$. In addition, in (23), the dimensionless gravity vector \mathbf{g} is merely the unit vector \mathbf{e}_{x_0} and $\pi/6$ stands for the dimensionless bubble volume.

The associated boundary conditions read

$$\mathbf{T} \cdot \mathbf{n} = \Sigma \mathbf{n} \quad \text{on} \quad \partial_b, \quad (26)$$

$$\mathbf{U} \cdot \mathbf{n} = \mathbf{W} \cdot \mathbf{n} \quad \text{on} \quad \partial_b, \quad (27)$$

$$\mathbf{U} = \mathbf{0} \quad \text{on} \quad \partial_{in}, \quad (28)$$

$$\mathbf{T} \cdot \mathbf{n} = \mathbf{0} \quad \text{on} \quad \partial_{out}, \quad (29)$$

where Σ is the dimensionless normal stress at the bubble surface. The formulation of the corresponding LSA problem is now slightly modified with respect to that described in Section II. The complete state vector for the fluid+bubble system is $\mathbf{Q} = [\mathbf{Q}^f, \mathbf{Q}^b]$, where \mathbf{Q}^f corresponds to the fluid unknowns already involved in the *fixed bubble* configuration, and $\mathbf{Q}^b = [\mathbf{V}, \mathbf{\Omega}, \mathbf{\Xi}]$ gathers the unknowns corresponding to the bubble degrees of freedom. Again the state vector is split into a base state \mathbf{Q}_0 and a linear perturbation \mathbf{q} . The base state corresponds to the steady vertical rise of the bubble with zero inclination ($\mathbf{Q}_0^b = [\mathbf{V}_0, \mathbf{0}, \mathbf{0}]$) while the disturbance is expanded in the normal mode form as

$$\mathbf{q} = [\hat{\mathbf{q}}^f(r, x)e^{im\theta}, \hat{\mathbf{q}}^b]e^{\lambda t}. \quad (30)$$

Injecting this decomposition into the linearized Navier-Stokes and Newton equations, the problem can be recasted into a generalized eigenvalue problem formally similar to that defined by (20). This procedure as well as the structure of the corresponding stiffness and mass matrices was detailed in Refs. 26 and 2 to which the reader is referred. Once these matrices have been built with FreeFem++, the linear system can be inverted, yielding the eigenvalues and the associated global modes of the fluid+bubble system. We run a large number of axisymmetric DNS with Gerris so as to obtain bubbles with a fore-aft asymmetric shape over a broad range of Ga and Bo (hence of Mo and Re). The LSA of each of these bubbles was then carried out in order to determine the corresponding neutral curve.

B. Results

We run series of Gerris simulations by keeping the Morton number fixed and varying the bubble equivalent diameter, i.e., varying Bo and Ga . This process was repeated for several values of Mo . The results corresponding to the LSA of the whole set of computed situations are gathered in Figure 7 which is probably the main result of this paper. It is first observed that the flow past a freely rising bubble is more unstable than that past a fixed bubble since, for a given Bo , the transition to instability always takes place at a lower Ga . However, the two neutral curves actually coincide in the range $1.2 \lesssim Bo \lesssim 5.5$ and it is mostly for both low and large Bond numbers that the fore-aft asymmetry makes a significant difference.

Unlike the case of fixed bubbles, the neutral curve corresponding to freely moving bubbles with Mo of $O(5 \times 10^{-7})$ exhibits a destabilization-restabilization behavior in the range $4.2 \lesssim Bo \lesssim 5.5$. Here, increasing the bubble size, i.e., Bo and Ga , the system first changes from stable to unstable, then restabilizes for some time until it becomes unstable again. Thus, for a given Bo in the above range, there exists regions where, as Ga is increased, the system recovers its stability after the base state has been found unstable. This destabilization-restabilization process was already noticed with freely moving solid disks and thin cylinders²⁶ and perfectly spheroidal bubbles.² It may be relevant to phase change and mass transfer situations in which the bubble size varies in time.

Figure 7 also shows, along with LSA results, data points collected from various experimental studies.^{8,12,13,27-29} Although the general trend revealed by these data is similar to that displayed by the theoretical neutral curve, most of them fall below the LSA prediction. This may have several

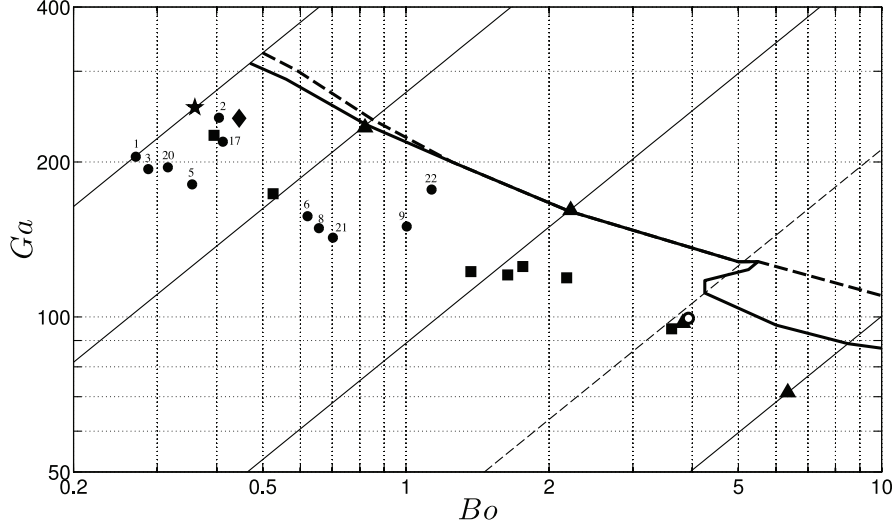


FIG. 7. Neutral curves obtained in the (Bo, Ga) plane using LSA with fore-aft asymmetric bubbles. The dashed and solid lines correspond to the fixed and freely moving configurations, respectively. Experimental data corresponding to incipient path instability observed in various liquids are also included (■, ²⁷★, ²⁸♦, ⁸▲, ¹²○, ¹³ and •, ²⁹ numbers associated with the latter data refer to those of Table 1 in Ref. 29). The thin solid (dashed) lines correspond to iso- Mo lines (from left to right): 1.109×10^{-11} (water under standard conditions), 1.8×10^{-10} , 1.6×10^{-8} , 9.9×10^{-6} (5×10^{-7}).

well distinct causes. First, it must be kept in mind that most experiments reported in Refs. 27 and 29 were carried out with polar liquids (water, mixtures involving water, and alcohols). At the time of these experiments and despite the care taken to purify these liquids, there were no means to eliminate entirely surfactants from them, so that the amount of contamination of the bubble surface is unknown. Since contamination is known to dramatically lower the critical Reynolds number (hence the Galilei number) of the transition,^{4,29} one can suspect that a good part of the shift between LSA predictions and experiments is due to this phenomenon. In contrast, experiments corresponding to Refs. 8 and 28 were carried out in ultrapure water, whereas those corresponding to Refs. 12 and 13 employed various silicon oils, and these are nonpolar liquids with which the bubble surface is easily kept clean. These are the two most stringent data sets to assess the validity and limitations of the LSA results. In pure water, transition to an unstable path has been reported to take place at $Re \approx 660$, i.e., $Ga \approx 246$.⁸ This is about 20% lower than the LSA prediction which, at the corresponding Bond number, indicates a critical Galilei number slightly larger than 300. The most likely reason for this difference is that at such large Re , neither the flow past the bubble nor the bubble shape itself reaches a strictly steady state. Starting from rest, the rise velocity goes on increasing, although slightly, until path instability occurs. Indeed, the diffusion time $t_v = \rho D^2 / \mu$ is much longer than the advective time $t_a = D / U_T$, so that physical processes governed by viscous diffusion, especially the development of the boundary layer and wake that result from vorticity generation at the bubble surface, have not come to an end at the time the bubble has almost reached its terminal velocity. Moreover, starting from rest with a spherical shape, the bubble is likely to experience shape oscillations and, in this high- Re regime, requires a long period of time to reach its final, nearly oblate, steady shape. In Ref. 30, it was shown that, in the case of a rising bubble that retains a nearly spherical shape, the characteristic damping time t_d of the dominant mode of shape oscillations is $t_d = \frac{1}{160} \rho D^2 / \mu$. Hence, the two ratios t_v / t_a and t_d / t_a increase linearly with Re . For instance, in Figure 7, these two ratios are 3.7 times larger at the critical point corresponding to water ($Mo = 1.109 \times 10^{-11}$, $Ga \approx 311$, $Bo \approx 0.47$) than at its counterpart in the case of the silicon oil with $Mo = 1.6 \times 10^{-8}$ ($Ga = 161$, $Bo \approx 2.20$), for which an excellent agreement with experiments is observed. This linear increase of t_v / t_a and t_d / t_a with Re makes the LSA approach based on a strictly steady base state questionable in the high- Re (hence low- Mo) regime.

Comparison of LSA results with data obtained in silicon oils shows an excellent agreement for the critical conditions corresponding to the smallest two values of the Morton number, i.e., to the range $0.8 \lesssim Bo \lesssim 2.2$. Here, the critical Reynolds number ranges from 467 to 240 and the flow past the bubble as well as the bubble shape have certainly reached a steady state before the instability

manifests itself. The situation is different with the highest two values of the Morton number, where the data clearly fall below the theoretical critical curve. The corresponding Bond numbers being of $O(4)$ or larger, we guess that here the frozen shape assumption is not tenable any more: since surface tension effects get weak, flow disturbances are likely to induce slight deformations of the bubble surface which in turn tend to accelerate the transition. In the worst case, i.e., for the highest value of the Morton number ($Mo = 9.9 \times 10^{-6}$), predicted values of the critical Galilei number differ from observations by about 30%.

To finish with this comparison, let us point out that another scenario might have explained discrepancies between LSA predictions and experiments, namely, the possible subcritical nature of the primary bifurcation, a situation that cannot be predicted by LSA. However, with spheroidal bubbles, DNS¹⁵ and properties of the normal form derived from the system of governing equations (21)-(24)³¹ confirmed the supercritical nature of the bifurcation throughout the whole range of aspect ratios covered by the LSA approach. Therefore, it would be very unlikely that a subcritical bifurcation exists with fore-aft asymmetric shapes which remain close to an oblate spheroid. The conclusion of this analysis is that the present LSA provides reliable quantitative predictions within a limited range of Bond numbers, typically $0.8 \leq Bo \leq 3-4$. Out of this range, present assumptions appear to be somewhat too restrictive. This was our main motivation to turn to the full DNS approach whose results will be discussed in a forthcoming paper.

Figure 8 reveals the variations of the dimensionless frequency $St = \lambda_i/2\pi$ along the critical curve. It turns out that, in contrast with the fixed-bubble situation where the first instability always occurs through a stationary bifurcation, the first unstable mode encountered with a freely moving bubble is generally oscillatory (i.e., the bifurcation is of Hopf type), yielding a periodic bubble path which may be planar (hence a zig-zag) or three-dimensional (a circular helix). A similar difference was noticed in Ref. 2 with spheroidal bubbles. However, in the intermediate range $1.2 \lesssim Bo \lesssim 5.5$, the primary bifurcation is still stationary, which yields a steady oblique bubble path beyond the threshold. This is why the two neutral curves corresponding to LSA predictions in Figure 7 coincide in this intermediate range. At higher Bo , the first unstable mode exhibits “high frequency” oscillations with $St = O(0.1)$. For $Bo \lesssim 1.2$, the primary bifurcation is again of Hopf type but the associated unstable mode exhibits “low-frequency” oscillations with $St = O(0.02)$. Similar behaviors have been found experimentally, being the low-frequency path oscillation identified in Ref. 7 at $Bo \approx 0.44$ or the high-frequency zig-zag reported in Ref. 13 at $Bo \approx 4$. The differences found between the experimental values of St and those predicted by the LSA are presumably due to the significant variations of the Strouhal number with the distance to the threshold, a shift that LSA can barely predict since it results in good part from nonlinear processes.

In order to facilitate the comparison of LSA results obtained with a fore-aft asymmetric bubble with those found with a perfectly spheroidal bubble, we also draw the two neutral curves in the (χ, Re) plane in Figure 9. The figure also shows, for completeness, the bubble shapes at six characteristic points along the neutral curve together with a table providing their coordinates (χ, Re)

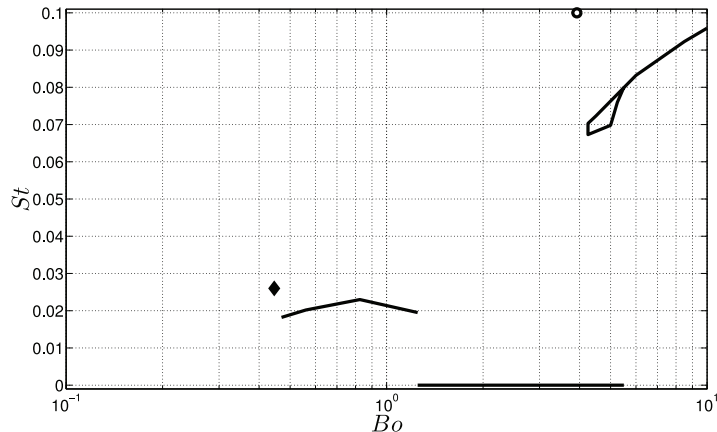


FIG. 8. Frequency diagram (Bo, St) provided by the LSA approach for a freely moving bubble with a fore-aft asymmetric shape, together with experimental data from Refs. 7 (◆) and 13 (○).

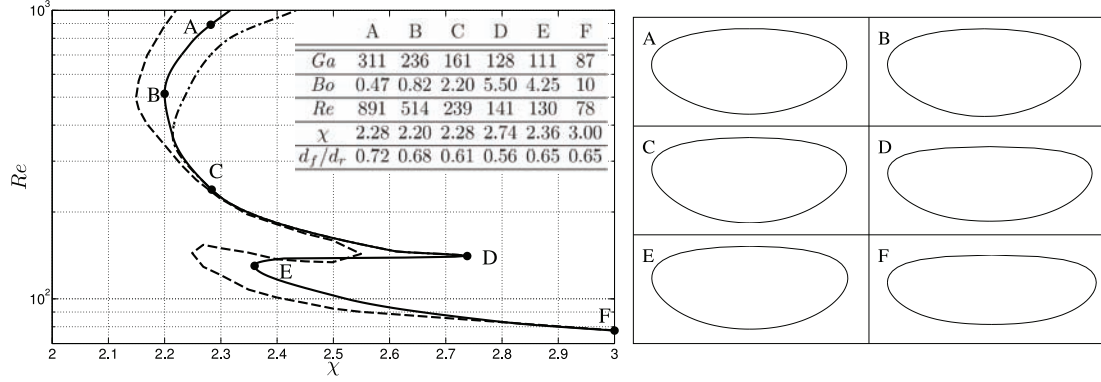


FIG. 9. Stability diagram of the flow about freely moving bubbles in the (χ, Re) plane. The solid and dashed lines correspond to the neutral curves obtained via LSA with a freely moving fore-aft asymmetric and a perfectly spheroidal bubble,² respectively. The dashed-dotted line corresponds to the neutral curve of a fixed, fore-aft asymmetric bubble (solid line in Figure 3); for $Re \lesssim 400$, it almost coincides with the part of the solid line that ends at point D. Bubbles shapes at points A-F are shown in the right part of the figure; the table in the left part provides the coordinates (χ, Re) and (Bo, Ga) of these points and the ratio d_f/d_r of the front and rear semi-axes lengths of the corresponding bubbles.

and (Bo, Ga) and the ratio of the front and rear semi-axes lengths, d_f/d_r . First, comparing with the corresponding neutral curve in Figure 3, it appears that the lower part of the neutral curve obtained in the case in which the bubble is free to move has dramatically shifted towards lower Re . For instance, the critical Reynolds number corresponding to $\chi = 2.5$ is about 190 in the fixed-bubble case, whereas it is close to 100, i.e., it is about two times smaller, with a freely moving bubble. Hence, as already mentioned, the flow about freely moving bubbles is generally significantly more unstable than that past fixed ones. What is specific to freely moving bubbles is the existence of the “high-frequency” branch that starts at the “trough” located at $\chi \approx 2.74$, $Re \approx 141$ and develops toward low Re . For increasing Reynolds numbers, this branch which has no counterpart in the fixed-bubble case provides the first bifurcation for bubbles with an aspect ratio larger than 2.36, i.e., a Bond number larger than 4.2. The comparison of the two neutral curves corresponding to freely moving bubbles in Figure 9 reveals both differences and similarities. Roughly speaking, the neutral curve is shifted towards the right, i.e., towards higher χ , when the shape asymmetry is taken into account. Hence, the main difference is that the flow past bubbles with a fore-aft asymmetry (hence their path) is slightly more stable than that past a perfectly spheroidal bubble with the same aspect ratio. In particular, it is seen that instability can only take place beyond a critical aspect ratio $\chi_c \approx 2.15$ with spheroidal bubbles, whereas this threshold is increased up to $\chi_c \approx 2.2$ with fore-aft asymmetric bubbles. However, one also observes that the global shape of the neutral curve is preserved, whether or not shape asymmetry is taken into account. Figure 10 also shows that all

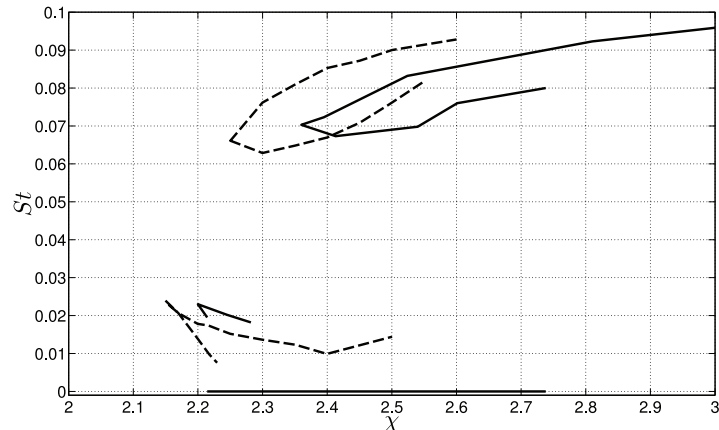


FIG. 10. Frequency diagram (χ, St) . Same convention as in Figure 9.

three branches of high, low, and zero frequency modes exist at quite similar locations in the (χ, St) plane for both bubble geometries; the associated frequencies are also close for both of them.

IV. CONCLUSIONS

In this work, we have studied the global linear stability of the wake and path of gas bubbles rising in a stagnant Newtonian liquid, focusing on the effect of the real bubble shape on the stability properties. We used a two-step approach. In the first step, the shapes and terminal velocities of the bubbles were obtained over a wide range of Galilei and Bond numbers from axisymmetric time-dependent numerical simulations implemented within Gerris Flow Solver. Then, we performed a global linear stability analysis, keeping the previously obtained shape frozen, along two different scenarios. On the one hand, we considered bubbles whose velocity and orientation were kept fixed; therefore, these bubbles interacted with the fluid only like fixed bodies. On the other hand, we considered bubbles free to move and rotate, which required the coupled fluid+bubble system of linearized governing equations to be solved.

As in the case of spheroidal bubbles, we found that the primary instability always occurs through a stationary bifurcation for fixed bubbles. We observed that, for sufficiently large Reynolds numbers, the flow past a fixed fore-aft asymmetric bubble is significantly more stable than that past a perfectly spheroidal bubble. Hence, the fact that real bubbles with a given aspect ratio exhibit a flatter front and a more rounded rear than the corresponding oblate spheroid has been proven to stabilize the wake, confirming recent results provided by a sensitivity analysis.¹ In contrast, virtually no difference was found between the two geometries for Reynolds numbers less than approximately 400, leaving the lower branch of the neutral curve almost unaffected by the shape asymmetry.

To be in position to perform a direct comparison with experimental results, we then extended the global linear stability analysis to freely rising bubbles with fore-aft asymmetry. As in the case of purely spheroidal bubbles, the neutral curve of the coupled fluid+bubble system was found to exhibit a much richer behavior than the fixed-bubble configuration. Indeed, the first instability arises through a Hopf bifurcation associated with a low-frequency mode ($St \approx 0.02$) at low Bond numbers (high Galilei numbers, i.e., $Ga \gtrsim 200$) and with a high-frequency mode ($St \approx 0.10$) at high Bond numbers (low Galilei numbers, i.e., $Ga = O(100)$), whereas it occurs through a stationary bifurcation in the intermediate range $1.2 < Bo < 5.5$. Compared to the flow past a perfectly oblate spheroidal bubble, that past a bubble with fore-aft asymmetry has been found to be more stable for both low (typically $\lesssim 1$) and large (typically $\gtrsim 5$) Bond numbers, whereas the asymmetry does not modify its stability in the intermediate range corresponding to the stationary bifurcation. For liquids with Morton numbers of $O(5 \times 10^{-7})$, there is a subregion in the range $4.2 < Bo < 5.5$ with no counterpart in the fixed-bubble configuration, where the flow becomes unstable beyond a critical Galilei number of $O(110)$, then restabilizes at slightly higher Galilei numbers until it eventually becomes unstable again beyond $Ga = O(130)$ (see Figure 7).

Present results clearly improve over those of Ref. 2 by considering realistic bubble shapes on which the normal stress balance is satisfied everywhere as far as the flow is steady and axisymmetric. However, consistent quantitative discrepancies with respect to recent experimental data obtained in uncontaminated liquids remain, regarding critical conditions in the low- and high- Bo ranges defined above. In the low- Bo range, we suspect that these discrepancies are due to the remaining unsteadiness of the base flow at the time the instability starts to manifest itself, a feature not taken into account in the present LSA where a strictly stationary base state is assumed. In the high- Bo range, small amounts of energy are sufficient to induce local changes in the bubble shape and it is likely that pressure disturbances associated with the onset of the instability result in significant shape disturbances whose effect on the stability of the whole system is not taken into account in the present LSA scheme. To overcome these limitations, we are currently following two distinct paths. First, we are exploring the possibility to incorporate effects of shape disturbances in the LSA procedure. Second, we are performing fully three-dimensional numerical simulations in which the above two restrictions are removed since the flow and the bubble shape are allowed to evolve all along the simulation. The corresponding results, primarily aimed at elucidating the

remaining differences observed here between LSA results and experimental measurements, will be discussed in a forthcoming paper.

ACKNOWLEDGMENTS

This work has been supported by the Spanish MINECO (Subdirección General de Gestión de Ayudas a la Investigación), Junta de Andalucía, and European Funds under Project Nos. DPI2014-59292-C3-3-P and P11-TEP-7495, respectively. J.C.C.-L. is grateful to the Interface Group at IMFT for their hospitality during his research stay.

- ¹ J. Tchoufag, J. Magnaudet, and D. Fabre, “Linear stability and sensitivity of the flow past a fixed oblate spheroidal bubble,” *Phys. Fluids* **25**, 054108 (2013).
- ² J. Tchoufag, J. Magnaudet, and D. Fabre, “Linear instability of the path of a freely rising spheroidal bubble,” *J. Fluid Mech.* **751**, R4 (2014).
- ³ R. Clift, J. R. Grace, and M. E. Weber, *Bubbles, Drops and Particles* (Academic Press, 1978).
- ⁴ J. Magnaudet and I. Eames, “The motion of high-Reynolds number bubbles in inhomogeneous flows,” *Annu. Rev. Fluid Mech.* **32**, 659–708 (2000).
- ⁵ P. Ern, F. Risso, D. Fabre, and J. Magnaudet, “Wake-induced oscillatory paths of bodies freely rising or falling in fluids,” *Annu. Rev. Fluid Mech.* **44**, 97–121 (2012).
- ⁶ M. K. Tripathi, K. C. Sahu, and R. Govindarajan, “Dynamics of an initially spherical bubble rising in quiescent liquid,” *Nat. Commun.* **6**, 6268 (2015).
- ⁷ P. C. Duineveld, “Bouncing and coalescence of two bubbles in water,” Ph.D. thesis, University of Twente, 1994.
- ⁸ P. C. Duineveld, “Rise velocity and shape of bubbles in pure water at high Reynolds number,” *J. Fluid Mech.* **292**, 325–332 (1995).
- ⁹ S. Takagi and Y. Matsumoto, “Surfactant effects on bubble motion and bubbly flows,” *Annu. Rev. Fluid Mech.* **43**, 615–636 (2011).
- ¹⁰ Y. Tagawa, S. Takagi, and Y. Matsumoto, “Surfactant effect on path instability of a rising bubble,” *J. Fluid Mech.* **738**, 124–142 (2014).
- ¹¹ J. Magnaudet and G. Mougin, “Wake instability of a fixed spheroidal bubble,” *J. Fluid Mech.* **572**, 311–337 (2007).
- ¹² R. Zenit and J. Magnaudet, “Path instability of rising spheroidal air bubbles: A shape-controlled process,” *Phys. Fluids* **20**, 061702 (2008).
- ¹³ R. Zenit and J. Magnaudet, “Measurements of the streamwise vorticity in the wake of an oscillating bubble,” *Int. J. Multiphase Flow* **35**, 195–203 (2009).
- ¹⁴ T. Sanada, K. Sugiyama, M. Shirota, and M. Watanabe, “Motion and drag of a single bubble in super-purified water,” *Fluid Dyn. Res.* **40**, 534–545 (2008).
- ¹⁵ G. Mougin and J. Magnaudet, “Path instability of a rising bubble,” *Phys. Rev. Lett.* **88**, 014502 (2002).
- ¹⁶ J. C. Cano-Lozano, P. Bohorquez, and C. Martínez-Bazán, “Wake instability of a fixed axisymmetric bubble of realistic shape,” *Int. J. Multiphase Flow* **51**, 11–21 (2013).
- ¹⁷ B. Yang and A. Prosperetti, “Linear stability of the flow past a spheroidal bubble,” *J. Fluid Mech.* **582**, 53–78 (2007).
- ¹⁸ S. Popinet, “Gerris: A tree-based adaptive solver for the incompressible Euler equations in complex geometries,” *J. Comput. Phys.* **190**, 572–600 (2003).
- ¹⁹ S. Popinet, “An accurate adaptive solver for surface-tension-driven interfacial flows,” *J. Comput. Phys.* **228**, 5838–5866 (2009).
- ²⁰ F. Hecht, “New development in FreeFem++,” *J. Numer. Math.* **20**, 251–265 (2012).
- ²¹ J. C. Cano-Lozano, R. Bolaños-Jiménez, C. Gutiérrez-Montes, and C. Martínez-Bazán, “The use of volume of fluid technique to analyze multiphase flows: Specific case of bubble rising in still liquids,” *Appl. Math. Model.* **39**, 3290–3305 (2015).
- ²² R. Verfürth, “Finite element approximation of incompressible Navier-Stokes equations with slip boundary condition II,” *Numer. Math.* **59**, 615–636 (1991).
- ²³ D. Sipp and A. Lebedev, “Global stability of base and mean flows: A general approach and its applications to cylinder and open cavity flows,” *J. Fluid Mech.* **593**, 333–358 (2007).
- ²⁴ E. Sanmiguel-Rojas, A. Sevilla, C. Martínez-Bazán, and J.-M. Chomaz, “Global mode analysis of axisymmetric bluff-body wakes: Stabilization by base bleed,” *Phys. Fluids* **21**, 114102 (2009).
- ²⁵ P. Bohorquez, E. Sanmiguel-Rojas, A. Sevilla, J. I. Jiménez-González, and C. Martínez-Bazán, “Stability and dynamics of the laminar wake past a slender blunt-based axisymmetric body,” *J. Fluid Mech.* **676**, 110–144 (2011).
- ²⁶ J. Tchoufag, D. Fabre, and J. Magnaudet, “Global linear stability analysis of the wake and path of buoyancy-driven disks and thin cylinders,” *J. Fluid Mech.* **740**, 278–311 (2014).
- ²⁷ H. Tsuge and S. I. Hibino, “The onset conditions of oscillatory motion of single gas bubbles rising in various liquids,” *J. Chem. Eng. Jpn.* **10**, 66–68 (1977).
- ²⁸ A. W. G. De Vries, “Path and wake of a rising bubble,” Ph.D. thesis, University of Twente, 2001.
- ²⁹ R. A. Hartunian and W. R. Sears, “On the instability of small gas bubbles moving uniformly in various liquids,” *J. Fluid Mech.* **3**, 27–47 (1957).
- ³⁰ J. M. Gordillo, B. Lalanne, F. Risso, D. Legendre, and S. Tanguy, “Unsteady rising of clean bubble in low viscosity liquid,” *Bubble Sci., Eng., Technol.* **4**, 4–11 (2012).
- ³¹ J. Tchoufag, D. Fabre, and J. Magnaudet, “Weakly nonlinear model with exact coefficients for the fluttering and spiraling motion of buoyancy-driven bodies,” *Phys. Rev. Lett.* **115**, 114501 (2015).